ARF6 is an important host factor for SARS-CoV-2 infection *in vitro*.

Mirabelli C.[1#], Sherman E.J.[2#], Wotring J.W.[3], El Saghir J.[4], Bragazzi Cunha J.[2], Harder J.[4], Sexton J.Z.[3], Emmer B.T.[2] and Wobus C.E.[1]*

[1]Department of Microbiology and Immunology, University of Michigan medical school, Ann Arbor (MI, USA
[2] Department of Internal Medicine, Division of Hospital Medicine, University of Michigan, Ann Arbor (MI), USA
[3] Department of Internal Medicine, Division of Gastroenterology and Hepatology, University of Michigan, Ann Arbor, Michigan, USA
[4]Department of Internal Medicine, Division of Nephrology, University of Michigan, Ann Arbor, Michigan, USA

[#]Current affiliation:

Mirabelli C., *Institut für Virologie und ZellBiologie, University of Lübeck, Germany*
Sherman E.J., *Territory Manager at Takara Bio USA, Inc. - MI, MN, IN, KY*

[*]Corresponding author: camirabe@med.umich.edu

Abstract

SARS-CoV-2 is a newly emerged beta-coronavirus that enter cells via two routes, direct fusion at the plasma membrane or endocytosis followed by fusion with the late endosome/lysosome. While the viral receptor, ACE2, multiple entry factors, and the mechanism of fusion of the virus at the plasma membrane have been extensively investigated, viral entry via the endocytic pathway is less understood. By using a human hepatocarcinoma cell line, Huh-7, which is resistant to the antiviral action of the TMPRSS2 inhibitor camostat, we discovered that SARS-CoV-2 entry is not dependent on dynasore but dependent on cholesterol. ADP-ribosylation factor 6 (ARF6) has been described as a host factor for SARS-CoV2 replication and it is involved in the entry and infection of several pathogenic viruses. By CRISPR-Cas9 genetic deletion, we found that ARF6 is important for SARS-CoV-2 uptake and infection in Huh-7. In addition, the ARF6 inhibitor NAV-2729, and the ARF6 agonist AA147, showed a dose-responsive inhibition or enhancement of viral infection, respectively. Importantly, ARF6 inhibition reduced SARS-

CoV-2 viral loads also in more physiologic models of infection: Calu-3 and kidney organoids, suggesting a role also in post-entry steps. Together, these experiments points to a ARF6 as a putative target to develop antiviral strategies against SARS-CoV-2.

Keywords: SARS-CoV-2, entry, ARF6, endocytic pathway, therapeutic targets

56 **Introduction**

57 SARS-CoV-2 is a newly emerged beta-coronavirus and causative agent of the COVID-19
58 pandemic. While several vaccines and antivirals have been approved to limit severe COVID-19,
59 the spread of the virus is not yet under control. This highlights the importance of developing
60 additional therapeutic strategies that can complement vaccine rollout, especially at the epidemic
61 centers. Given the propensity of RNA viruses for development of drug resistance, there is an
62 unmet need for further antiviral compounds that can curb the infection and transmission by
63 targeting additional steps in the virus life cycle. Viral entry is a step in the viral cycle that is
64 promising for antiviral development and has been characterized very early after the isolation of
65 SARS-CoV-2, with the discovery of the uncoating receptor, ACE2[1] and the two entry pathways
66 [2]: via plasma membrane fusion or endocytosis. Membrane fusion at the plasma membrane occurs
67 after SARS-CoV-2 surface (S) protein activation by proteinase cleavage, including TMPRRS2,
68 whereas fusion in the endocytic compartment requires the intracellular protease cathepsin L. The
69 pathway and molecular players that govern endocytosis-mediated entry are however poorly
70 characterized. Endocytosis of viruses can occur via different pathways, including clathrin-
71 mediated endocytosis (CME), caveolar or lipid raft-mediated endocytosis, macropinocytosis and
72 variations of these themes[3]. Some viruses are able to use more than one pathway, which
73 introduces a further level of ambiguity to the classification of virus entry pathways. Research on
74 SARS-CoV-2 endocytic-mediated entry has been scant. A single report using a lentivirus system
75 in ACE-2 overexpressing 293T cells suggests that SARS-CoV-2 endocytosis is dependent on
76 clathrin and dynamin[4]. However, no further studies on SARS-CoV-2 endocytic entry pathway
77 have been performed, particularly in the context of a productive infection.

78 ADP-ribosylation factor 6 (ARF6) is a multi-functional cellular protein. It directly activates lipid
79 modifying enzymes, such as phosphatidylinositol 4-phosphate 5-kinase, and it stimulates actin
80 polymerization. ARF6-positive cargoes can be directly transported on microtubule filaments; and
81 it also assists autophagy, particularly the initiation and autophagosome formation[5]. Because of its
82 roles in endocytosis and trafficking, ARF6 is co-opted by several pathogens; bacteria (e.g.,
83 enteropathogenic and enterohemorrhagic *Escherichia coli*, *Salmonella Typhimurium, Shigella*)
84 and viruses (e.g., HIV-1, Coxsackievirus A and B, Epstein Barr virus). ARF6 was recently
85 identified as a cellular partner of the uridine-specific endoribonuclease Nsp15 of SARS-CoV-2[6],
86 and according to a recent re-analysis of a RNA sequencing dataset of infected A549-ACE2 cells,
87 ARF6 is involved in three of the four identified modules mediating host cell responses during
88 SARS-CoV-2 infection, i.e., viral entry, regulation and signaling, and immune responses[7]. We
89 therefore sought out to determine the role of ARF6 in SARS-CoV-2 endocytosis and, more
90 broadly, infection.
91 We first found that the human hepatocarcinoma cell line, Huh-7 is resistant to camostat, a
92 specific TMPRSS2 inhibitor, and hence SARS-CoV-2 entry mostly relies on endocytosis for
93 infection. By genetic depletion and pharmacologic inhibition, we further demonstrated that
94 SARS-CoV-2 entry into Huh-7 is dynamin-independent but dependent on cholesterol and ARF6.
95 This host factor is also important for infection in the more physiologic relevant models of human
96 lung Calu3 cells and kidney organoids, suggesting that ARF6 might be an effective therapeutic
97 target.
98
99
100

101 **Material and Methods**

102 **Cells and virus.** Human hepatocarcinoma cells, Huh-7, and human lung adenocarcinoma cells,
103 and Calu3, were obtained by collaborators and maintained at 37 °C and 5% CO2 in Dulbecco's
104 modified Eagle's medium (DMEM) (Gibco), supplemented with 10% heat-inactivated fetal
105 bovine serum (FBS), Hepes, nonessential amino acids, L-glutamine, and 1× Pen-Strep (Gibco).
106 SARS-CoV-2 was obtained through BEI Resources (SARS-Related Coronavirus 2, Isolate USA-
107 WA1/2020, NR-52281 and Isolate hCoV-19/USA/GA-EHC-2811C/2021 [Omicron
108 Variant] NR-56481). Lack of genetic drift of our viral stock was confirmed by deep sequencing.
109 Viral titers were determined by $TCID_{50}$ assays in Vero E6 cells (Reed and Muench method). All
110 experiments using SARS-CoV-2 were performed at the University of Michigan under Biosafety
111 Level 3 (BSL3) protocols in compliance with containment procedures in laboratories approved
112 for use by the University of Michigan Institutional Biosafety Committee and Environment,
113 Health and Safety.

114 **SARS-CoV-2 infection and quantification by immunofluorescence.** Cells were seeded at
115 3,000 cells/well (384-well plate, Perkin-Elmer, 6057300) or 10,000 cells/well (96-well plates,
116 Costar, 3916) and allowed to adhere overnight. Compounds were then added to the cells and
117 incubated for 2 hrs at 37 °C. Plates were then transferred to BSL3 containment and infected with
118 SARS-CoV-2 WA1 or Omicron at a MOI of 1. After 1 h of absorption, the virus inoculum was
119 removed and fresh media with inhibitors was added. Uninfected and vehicle-treated infected
120 cells were included as negative and positive controls, respectively. Plates were then stained as
121 previously described[8] by using anti-nucleocapsid protein (anti-N) SARS-CoV-2 antibody
122 (Antibodies Online; catalog no. ABIN6952432) followed by staining with secondary antibody
123 Alexa-647 (goat anti-mouse; Thermo Fisher; A21235) and DAPI for nuclei staining. Stained

124 cells were acquired on Thermo Fisher CX5 high-content microscopes with a 20×/0.45 N.A.
125 LUCPlan FLN objective. Laser autofocus was performed and 9 or 18 fields per well were
126 imaged covering ~80% of the well area. Images were analyzed with Cell Profiler software and
127 percent of infected cells (N-positive) was calculated on the total cell count (i.e., DAPI positive).
128 **SARS-CoV-2 infection and quantification by $TCID_{50}$ assay.** 200,000 Huh-7 or Huh-7 knock-
129 out (KO) cells were seeded in 12-well plates. For the Calu-3, 100,000 cells were seeded in 24-
130 well plates. The next day or at 80% cell confluency, compounds were added to the cells and
131 incubated for 2 hrs. Cells were then infected with SARS-CoV-2 WA1 at a MOI of 1 for 1 h at 37
132 °C Inoculum was removed, cells were washed 3 times with PBS without Magnesium and
133 Calcium (PBS-/-) and fresh medium was added. Cells were harvested 1 day post infection (dpi)
134 and lysates were obtained by one cycle of freeze-thaw. SARS-CoV-2 infection was quantified by
135 $TCID_{50}$ on pre-seeded Vero E6 cells (Reed and Muench method) or by RT-qPCR (IDT
136 technologies, Charité kit) after RNA extraction with TRI reagent and Direct-Zol RNA miniprep
137 kit (Zymo Research).
138 **Generation of CRISPR-KO cell lines.** Individual guide RNA (gRNA) sequences
139 (Supplemental Table 1) were cloned into BsmBI-digested lentiCRISPRv2 (Addgene #52961, a
140 gift from Feng Zhang[9]) and resulting lentiviral stocks prepared as previously described[10]. Huh-7
141 and Calu-3 cells were transduced with lentiviral stocks at an MOI of ~1, treated 1 day later with
142 puromycin (3 ug/mL) until death of control uninfected cells was complete, and passaged as
143 needed to maintain logarithmic phase growth for 2-3 weeks. Cells were then either harvested for
144 mRNA and protein preparations or infected with SARS-CoV-2 infection as described above.
145 **Western blot.** Cells were lysed in RIPA buffer (Pierce, 89900) with PhosSTOP (Roche,
146 04906845001) and cOmplete EDTA-free protease inhibitor cocktail (Roche, 11873580001) on

147 ice. After vortexing to ensure a complete lysis, cells were centrifuged at 4°C, 14,000 × g for 15
148 min. The supernatant was mixed with β-mercaptoethanol-containing (10%) Laemmli buffer
149 (Bio-Rad, cat nr. 1610747) at 3:1 ratio and denatured at 90°C for 10 min with a heat block.
150 Samples were spun down before being loaded in a 4 to 20% Mini-Protean TGX gels (Bio-rad,
151 number 456-1096). Gels were run at 80 to 100 V for 45 min to 1 h and transferred to Immobilon-
152 FL transfer membranes (IPFL00010) using semidry transfer at 10 V for 45 min. Membranes
153 were blocked in 5% bovine serum albumin fat-free milk prepared in PBS containing 0.05%
154 Tween 20 for a minimum of 2 hrs at room temperature. Membranes were incubated with primary
155 antibodies (anti-rabbit polyclonal ARF6 antibody, MyBioSource, cat nr. MBS822293 and anti-
156 mouse β–actin, 8H10D10, Cell Signaling, cat nr. 3700S) at 4°C by rocking overnight. Antibodies
157 were washed off the membranes with four 15-min rocking periods using fresh changes of PBS.
158 Secondary antibody incubation was done using fluorescent LI-COR antibodies (goat anti-rabbit
159 IgG, cat. nr. 926-68071; and goat anti-mouse IgG, cat nr. 926-32210) diluted 1:10,000 in PBS
160 for 1 hr at room temperature with gentle rocking. Membranes were washed with PBS as before
161 and visualized using a LI-COR Odyssey Imager.
162 **Viability assay.** Huh-7 cells were seeded in a 96-well plate at 10,000 cells/well and allowed to
163 adhere overnight. The next day, medium was replaced by medium with compounds or vehicle
164 (DMSO, at the highest concentration used) and resazurin (Biotium, 30025-1) was added
165 according to the manufacturer´s instruction. One day post treatment (to mimic infection
166 condition), absorbance (590 nm) was measured with a Synergy™ HTX plate reader.
167 **Attachment/internalization assay.** Huh-7 or ARF6-KO cells were plated in 48-well plates at
168 100,000 cells per well and allowed to adhere overnight. The following day, NAV-2729 was
169 added at the indicated concentration and incubated for 2 hrs. Following compound incubation,

170 cells were infected with SARS-CoV-2 at an MOI of 10 for 1 h at 4 °C to allow for viral binding.
171 Cells were then washed three times with ice-cold PBS-/- to remove unbound virus, and harvested
172 in TRI reagent. Another set of treated-infected cells was transferred at 37°C to allow for viral
173 internalization. One hour after incubation, cells were treated with trypsin to remove bound-not
174 internalized virus and after centrifugation at 500 x g for 5 min, cells were harvested in TRI
175 reagent. RNA was extracted by using the Direct-Zol RNA miniprep kit (Zymogen; R2052) and
176 viral RNA was quantified by RT-qPCR. Proportion of internalized virus was calculated over the
177 bound virus.
178
179 **Results**
180 **SARS-CoV-2 infection in Huh-7 is resistant to camostat treatment but sensitive to Z-FA-**
181 **FMK.**
182 To investigate SARS-CoV-2 endocytosis, we screened a range of cell lines for the antiviral
183 activity of camostat mesylate, a specific inhibitor of TMPRSS2 (data not shown). Infection
184 readout was carried out with an imaging-based pipeline by using a SARS-CoV-2 anti-
185 nucleocapsid (N) antibody to detect infected cells. Interestingly, the human hepatocarcinoma cell
186 line Huh-7, was completely resistant to the antiviral action of camostat (**Figure 1A**). In contrast,
187 treatment with the irreversible cysteine protease inhibitor Z-FA-FMK, an inhibitor of the
188 intracellular protease cathepsin L, resulted in a strong antiviral activity with EC_{50} of 11 nM
189 (**Figure 1B**)[8]. Representative images are available in **Figure 1C**. These data suggest that SARS-
190 CoV-2 entry into Huh-7 cells is likely mediated by endocytosis and not membrane fusion.
191 Therefore, Huh-7 cells represent a model cell line to mechanistically study SARS-CoV-2
192 endocytic entry.

193 **SARS-CoV-2 uptake into Huh-7 cells is dynamin-independent**

194 A previous report with a lentivirus system in ACE-2 overexpressing 293T cells, suggests that
195 SARS-CoV-2 endocytosis is dependent on clathrin and dynamin[4]. We therefore determined if
196 dynamin governs SARS-CoV-2 entry into Huh-7 cells by using dynasore, a specific GTPase
197 inhibitor of dynamin I, II and Drp1 (the mitochondrial dynamin)[11]. ß-methyl cyclodextrin, a
198 cholesterol-removing agent that mostly blocks formation of lipid rafts important for endocytosis,
199 was used as a positive control since ACE2 is present in lipid rafts[12] and SARS-CoV entry is
200 dependent on cholesterol[13]. Huh-7 cells were pretreated 2 hrs prior to infection with selected
201 compounds at non-toxic concentrations (**Supplementary figure 1**) and infection with SARS-
202 CoV-2 was quantified by N protein expression. As expected, treatment with ß-methyl
203 cyclodextrin blocked viral infection. However, in contrast with previous findings, treatment with
204 the specific dynamin inhibitor dynasore, revealed a significant increase in the percentage of
205 infected cells (**Figure 2)**. This observation points to a clathrin-independent but cholesterol-
206 dependent endocytic uptake mechanism of SARS-CoV-2 into Huh-7 cells.

207

208 **Genetic perturbation of ARF6 results in a reduction of percentage of infected cells but not**
209 **of infectious titers.**

210 Dynamin-independent pathways are governed by the Rho GTPase-activating protein 26 (GRAF-
211 1), flotillin (FLOT-1) or ADP-ribosylation factor 6 (ARF6)[14]. Since ARF6 was recently
212 described for mediating host cell responses during SARS-CoV-2 infection, we generated two
213 polyclonal populations of CRISPR-targeted cells with gRNAs specific for ARF6 (c1 and c2).
214 ARF6 depletion was confirmed by RT-qPCR, whereby the efficacy of knock-down (KO) was
215 measured as a percentage of mRNA target gene expression compared to the non-targeting guide

216 (NTg) Huh-7 cell line (for clone 1, c1=39% and c2=56%) and by Western blot (**Supplementary**
217 **figure 2**). To test the efficacy of the CRISPR pipeline, ACE2-KO Huh-7 line was generated in
218 parallel as a control. Cells were infected with SARS-CoV-2 at MOI of 1 and harvested 1 dpi. A
219 combination of $TCID_{50}$ assay and RT-qPCR were used to quantify viral infection and replication,
220 respectively (**Figure 3A and 3B**). No significant differences were detected by $TCID_{50}$ between
221 ARF6 KO and NTg whereas replication was under the limit of detection for the ACE2-KO Huh-
222 7 cells. To independently validate these findings, an imaging-based readout for SARS-CoV-2
223 infection was used, since it is usually more sensitive than traditional infectivity assays. The assay
224 was adjusted to a 1dpi readout by infecting cells with SARS-CoV-2 at an MOI of 10. For ease of
225 experimentation, only ARF6-KO c1, with lower expression of the target gene was used for this
226 analysis. Representative images at 1 dpi are shown in **Figure 3C**. Intriguingly, we observed a
227 significant decrease in the percentage of infected cells in ARF6 KO than the NTg cells,
228 suggesting that ARF6 might be involved in SARS-CoV-2 entry (**Figure 3C**). Collectively, these
229 data suggest a role for ARF6 in SARS-CoV-2 infection in Huh-7.
230
231 **Pharmacologic inhibition of ARF6 blocks SARS-CoV-2 internalization**
232 ARF6 has been the object of extensive studies and specific small molecule inhibitors or agonist
233 are available commercially. We selected the inhibitor NAV-2729 and the agonist AA147 to test
234 their effect on SARS-CoV-2 infection. Huh-7 cells were pre-treated with a 1:2 dilution series of
235 compounds and infected with SARS-CoV-2 at MOI of 1. NAV-2729 showed a dose-response
236 inhibition of infection (**Figure 4A**), while AA147-treated cells showed increased infection
237 (**Figure 4B**), suggesting that ARF6 is a crucial factor for SARS-CoV-2 infection in Huh-7. We
238 next selected an efficacious non-toxic concentration of NAV-2729 to confirm inhibition by

239 $TCID_{50}$ (**Supplementary figure 1**). Intriguingly, treatment with NAV-2729 resulted in a 3-Log
240 reduction in viral infection in the NTg control. Treatment of the ARF6-KO with dynasore did not
241 result in changes of infection, further corroborating that dynamin is not involved in SARS-CoV-
242 2 endocytosis in Huh-7 (**Figure 4C**). To determine whether the NAV-2729 inhibitor worked at
243 the level of viral internalization, an attachment/internalization assay was performed. Briefly,
244 NTg cells were pre-treated with NAV-2729 and infected with SARS-CoV-2 at the MOI of 10.
245 ARF6-KO cells were included as a control. One hour post-inoculation on ice, cells were washed
246 and a set was harvested to quantify the virus attached at the cell surface. The other batch was
247 incubated at 37ºC for 1 hr to allow viral internalization, and after a treatment with trypsin to
248 remove unbound virus, cells were harvested to quantify the internalized virus by RT-qPCR.
249 NAV-2729 reduced viral internalization by 75% *versus* the more modest 25% observed in the
250 ARF6-KO, suggesting that ARF6 is a factor that governs endocytosis in Huh-7.
251
252 **ARF6 is an important host factor for SARS-CoV-2 infection in more physiological relevant**
253 **infection models**
254 Since ARF6 might play a role also in post-entry steps, we used the ARF6 inhibitor NAV-2729 in
255 other, more physiologic relevant models that are sensitive to camostat: the human renal
256 organoids and the human lung Calu-3 cell line[15]. In both models, treatment with NAV-2729
257 resulted in a significant reduction of viral replication (**Figure 5A and 5B**). The nucleoside
258 inhibitor remdesivir was used as a control. In addition, we performed CRISPR-Cas9 knockout of
259 ARF6 in Calu-3 cells to confirm that the inhibitory effect of NAV-2729 was ARF6-specific.
260 Infection with SARS-CoV-2 at an MOI of 1 was less efficient in the Calu3 line transduced with
261 the ARF6-targeting guide (ARF6) than in Calu-3 cells transduced with a non-targeting RNA

262 guide (NTg) (**Figure 5B**). The decrease in SARS-CoV-2 infection in Calu3 ARF6-KO cells was
263 more pronounced than in Huh-7 ARF6 KO cells (compare **Figure 5B** with **Figure 3B**),
264 suggesting that ARF6 might play additional roles in Calu-3 cells compared to Huh-7. Lastly, to
265 shed more light on the mechanism by which ARF6 assists SARS-CoV-2 replication in Calu-3
266 cells, we infected NTg and ARF6 KO Calu-3 cells with SARS-CoV-2 Omicron variant. This
267 variant has been demonstrated to rely primarily on endocytosis and not on membrane fusion for
268 entry *in vitro* and *in vivo*[16]. Both virus isolates were pre-treated with trypsin prior to infection.
269 Under these conditions, infection of NTg Calu-3 cells with SARS-CoV-2 Omicron resulted in
270 ~15-fold higher infection (as measured by % of N-positive cells at 24 hpt) than with the WA1
271 strain (**Figure 5C**). Infection of ARF6 KO with both strains showed a dramatic reduction
272 compared to NTg cells, suggesting that ARF6 might play a role in post-entry steps in Calu-3
273 cells. Overall, these results point to the importance of ARF6 in SARS-CoV-2 infection and to a
274 putative therapeutic target against coronavirus infection.
275

276 **Discussion**

277 In this study, we uncovered that ARF6 is a critical player of SARS-CoV-2 infection in cells of
278 liver, lung and kidney origin. In addition, in Huh7 cells, ARF6 inhibited SARS-CoV-2 uptake
279 with a mechanism that is further dependent on cholesterol but independent of dynamin and by
280 extension clathrin-independent. This is consistent with a manuscript that exclude the
281 involvement of dynamin, clathrin, caveolin and endophilin A2 for entry of SARS-CoV-2[13] and
282 with the entry pathway identified for SARS-CoV, which is cholesterol-dependent but clathrin-
283 and caveolin-independent[17]. However, our finding differs from a study demonstrating the
284 importance of clathrin in SARS-CoV-2 entry[4]. That study was performed with a lentivirus

285 system in 293T cells and not in the context of SARS-CoV-2 infection. Thus, differences in virus
286 and/or cell type may alter the endocytic uptake pathway.
287 Intriguingly, we observed that CRISPR-depleted cells exhibited a less pronounced phenotype as
288 compared with those treated with the ARF6 specific inhibitor, NAV-2729. This could be due to
289 several reasons. Because these cells are deficient for a crucial endocytic pathway and because
290 endocytic pathways are redundant, prolonged passaging of the ARF6-KO cells and the potential
291 incomplete activity of the guide RNA as indicated by the qPCR data might have led to
292 compensatory mechanisms and a less uniform phenotype. In contrast, the short-term treatment
293 with a small molecule inhibitor at non-toxic concentrations does not affect or modify the
294 physiology of the cell and reduce the impact of compensatory mechanisms and could thus be
295 more relevant for the study of these redundant endocytic pathways. The data on the lack of effect
296 of dynasore on ARF6-KO line (**Figure 5C**) further corroborate that in our model dynamin is not
297 involved in SARS-CoV-2 entry, regardless the penetrance of our CRISPR-KO strategy.
298 In our investigation, we expanded on the importance of ARF6 also in the context of infection of
299 other cell types; kidney organoids and Calu3 cells, a model of respiratory epithelial cells. In both
300 systems, the ARF6 inhibitor, NAV-2729, showed a strong antiviral effect. Since these cell
301 models support SARS-CoV-2 entry also via membrane fusion[18], these data indicate that ARF6 is
302 an important host factor also in post-entry steps. We confirmed that the inhibitory effect of
303 NAV-2729 in Calu3 was via ARF6 by CRISPR-Cas9 KO. ARF6-KO Calu3 exhibited a more
304 pronounced reduction of infection by both immunofluorescence and $TCID_{50}$ compared to the
305 ARF6 KO Huh7. This corroborates the hypothesis that in the Calu3 background, ARF6 is an
306 important host factor in post-entry steps.

307 It is not known what proportion of SARS-CoV-2 virions is entering via membrane fusion or
308 endocytosis *in vivo*. SARS-CoV-2 prefers activation by TMPRSS2 but if the target cells express
309 insufficient TMPRSS2 or if a virus–ACE2 complex does not encounter TMPRSS2, ACE2-bound
310 virus is internalized via endocytosis[2]. TMPRSS2 is found in the gastrointestinal, respiratory and
311 urogenital epithelium but not in other extra-mucosal compartments (i.e., heart, liver, kidneys,
312 brain, spleen and lymph nodes), where virus RNA or antigen is found in severe and deadly cases
313 of COVID-19, suggesting that entry and replication of SARS-COV-2 in these organs might be
314 exclusively driven by endocytosis. It is also possible that SARS-CoV-2 entry occurs by plasma
315 membrane fusion and endocytosis, regardless of the compartment. Therefore, it would be of
316 interest to use NAV-2729 in a small animal model to investigate the *in vivo* relevance of the
317 endocytic pathway and its importance in driving severe disease. Altogether, these data highlight
318 ARF6 as a potential target in the development of therapeutics against COVID-19. Future studies
319 focusing on ARF6-targeting investigational drugs, such as Linsitinib that has antiviral activity in
320 a pseudovirus assay[7], could hold promise for the development of additional SARS-CoV-2
321 therapeutics.
322
323 **Acknowledgements:** We thank Dr. A. Lauring (University of Michigan) for deep sequencing of
324 the viral stock. The work was in part funded by the University of Michigan Biological Science
325 Scholars Program to C.E.W. C.M. was supported by the Marie-Skłodowska-Curie Actions action
326 global fellowship (GA 841247). JZS is supported by the National Institute of Diabetes and
327 Kidney Diseases (R01DK120623) and National Center for Advancing Translational Sciences
328 Grant UL1TR002240. J.W.W. is supported by the Pharmacological Sciences Training Program
329 T32 Training Grant GM007767.

330 **Reference**

331 1 Hoffmann M, Kleine-Weber H, Schroeder S *et al.* SARS-CoV-2 Cell Entry
332 Depends on ACE2 and TMPRSS2 and Is Blocked by a Clinically Proven Protease
333 Inhibitor. *Cell* 2020. doi:10.1016/j.cell.2020.02.052.

334 2 Jackson CB, Farzan M, Chen B, Choe H. Mechanisms of SARS-CoV-2 entry into
335 cells. Nature Reviews Molecular Cell Biology. 2021. doi:10.1038/s41580-021-
336 00418-x.

337 3 Mercer J, Schelhaas M, Helenius A. Virus entry by endocytosis. Annual Review of
338 Biochemistry. 2010; **79**. doi:10.1146/annurev-biochem-060208-104626.

339 4 Bayati A, Kumar R, Francis V, McPherson PS. SARS-CoV-2 infects cells after
340 viral entry via clathrin-mediated endocytosis. Journal of Biological Chemistry.
341 2021; **296**. doi:10.1016/j.jbc.2021.100306.

342 5 Acker T van, Tavernier J, Peelman F. The small GTPase Arf6: An overview of its
343 mechanisms of action and of its role in host- pathogen interactions and innate
344 immunity. *International Journal of Molecular Sciences* 2019; **20**.
345 doi:10.3390/ijms20092209.

346 6 Gordon DE, Jang GM, Bouhaddou M *et al.* A SARS-CoV-2-Human Protein-
347 Protein Interaction Map Reveals Drug Targets and Potential Drug-Repurposing.
348 *bioRxiv* 2020. doi:10.1101/2020.03.22.002386.

349 7 Chen F, Shi Q, Pei F *et al.* A systems-level study reveals host-targeted repurposable
350 drugs against SARS-CoV-2 infection. *Molecular Systems Biology* 2021; **17**.
351 doi:10.15252/msb.202110239.

352 8 Mirabelli C, Wotring JW, Zhang CJ *et al.* Morphological cell profiling of SARS-
353 CoV-2 infection identifies drug repurposing candidates for COVID-19. *Proc Natl*
354 *Acad Sci U S A* 2021; **118**. doi:10.1073/pnas.2105815118.
355 9 Sanjana NE, Shalem O, Zhang F. Improved vectors and genome-wide libraries for
356 CRISPR screening. Nature Methods. 2014; **11**. doi:10.1038/nmeth.3047.
357 10 Emmer BT, Sherman EJ, Lascuna PJ, Graham SE, Willer CJ, Ginsburg D.
358 Genome-scale CRISPR screening for modifiers of cellular LDL uptake. *PLoS*
359 *Genetics* 2021; **17**. doi:10.1371/JOURNAL.PGEN.1009285.
360 11 Macia E, Ehrlich M, Massol R, Boucrot E, Brunner C, Kirchhausen T. Dynasore, a
361 Cell-Permeable Inhibitor of Dynamin. *Developmental Cell* 2006; **10**.
362 doi:10.1016/j.devcel.2006.04.002.
363 12 Sviridov D, Miller YI, Ballout RA, Remaley AT, Bukrinsky M. Targeting Lipid
364 Rafts—A Potential Therapy for COVID-19. *Frontiers in Immunology* 2020; **11**.
365 doi:10.3389/fimmu.2020.574508.
366 13 Li X, Zhu W, Fan M *et al.* Dependence of SARS-CoV-2 infection on cholesterol-
367 rich lipid raft and endosomal acidification. *Computational and Structural*
368 *Biotechnology Journal* 2021; **19**. doi:10.1016/j.csbj.2021.04.001.
369 14 Mayor S, Parton RG, Donaldson JG. Clathrin-independent pathways of
370 endocytosis. *Cold Spring Harbor Perspectives in Biology* 2014; **6**.
371 doi:10.1101/cshperspect.a016758.
372 15 Shang J, Wan Y, Luo C *et al.* Cell entry mechanisms of SARS-CoV-2. *Proc Natl*
373 *Acad Sci U S A* 2020; **117**. doi:10.1073/pnas.2003138117.

374 16 Pia L, Rowland-Jones S. Omicron entry route. *Nature Reviews Immunology* 2022.
375 doi:10.1038/s41577-022-00681-9.
376 17 Wang H, Yang P, Liu K *et al.* SARS coronavirus entry into host cells through a
377 novel clathrin- and caveolae-independent endocytic pathway. *Cell Research* 2008;
378 **18**. doi:10.1038/cr.2008.15.
379 18 Koch J, Uckeley ZM, Doldan P, Stanifer M, Boulant S, Lozach P. TMPRSS2
380 expression dictates the entry route used by SARS-CoV-2 to infect host cells. *The*
381 *EMBO Journal* 2021; **40**. doi:10.15252/embj.2021107821.
382

383 **Figure legends**

384 **Figure 1:** Huh-7 cells are resistant to the antiviral effect of camostat mesylate. A-B) Dose-
385 response curves of camostat mesylate (A) and the cathepsin B inhibitor Z-FA-FMK (B). Huh-7
386 cells were pre-treated with compound and infected with SARS-CoV-2 at MOI of 1 for 1h at
387 37'C. 48 hpi cells were fixed and permeabilized and stained with anti-N antibody. Cells were
388 imaged with high content imaging platform CX5 and analyzed with Cell profiler for image
389 segmentation. The % of infected cells were normalized to the non-treated infected condition.
390 Graph represents average SD of N=3 independent experiments with n=3 technical replicate,
391 each. C) Representative images of Huh-7 cells infected with SARS-CoV-2 or infected/treated
392 with Camostat (500 nM) and Z-FA-FMK (500 nM). N protein staining is represented in magenta,
393 nuclei are in blue.

394 **Figure 2:** Screening of inhibitors of the dynamin-dependent entry pathways in Huh-7 cells. Huh-
395 7 cells were pre-treated with compounds at the indicated concentration and infected with SARS-
396 CoV-2 at MOI of 1 for 1 h at 37ºC. 24 hpi cells were fixed, permeabilized and stained with anti-

397 N antibody. Cells were imaged with high content imaging platform CX5 and analyzed with Cell
398 profiler for image segmentation.
399 **Figure 3:** Genetic depletion of ARF6 does not affect viral titers but reduce the percentage of
400 infected cells A-B) Viral titer determination of SARS-CoV-2-infected NTg, ACE2-KO ARF6-
401 KO Huh7 clones (MOI of 1) by $TCID_{50}$/ml at 24 and 48 hpi (A) and by RT-qPCR at 24dpi (B).
402 ACE2-KO was used as a negative control of infection. Viral infectious titer was determined by
403 $TCID_{50}$ on Vero E6 cells. Dashed line represents the limit of detection of the $TCID_{50}$ assay. C)
404 Representative images of SARS-CoV-2-infected NTg and KO-Huh7 clones (MOI of 10). N
405 protein staining is represented in magenta, nuclei are in blue (DAPI). The graph represents the
406 quantification of SARS-CoV-2 infected cells (MOI of 10) at 24 hpi. Cells were imaged with high
407 content imaging platform CX5 and analyzed with Cell profiler for image segmentation. The % of
408 infected cells was normalized to the non-treated infected condition. Graph represents average SD
409 of N=3 independent experiments with n=3 technical replicate, each.
410 **Figure 4.** ARF6 is important during SARS-CoV-2 internalization in Huh-7 cells**.** A-B) NAV-
411 2729, an ARF6 inhibitor, and AA147, an ARF6 agonist, were used to pre-treat Huh-7 cells in a
412 384-well plate 2 hrs prior infection with SARS-CoV-2 (MOI of 1). Cells were harvested 48 hpi
413 and subjected to the imaging pipeline for viral quantification. 1:2 dose response curves were
414 performed in triplicate with 3 technical replicates, each. C) NTg Huh-7 were pre-treated with
415 NAV-2927 (10 μM) and ARF6 KO were pre-treated with dynasore (10 μM) for 2 h before
416 infection with SARS-CoV-2 (MOI of 1). Virus inoculum was removed 1 hpi and cells were
417 incubated with fresh medium +/- compounds. Cells were harvested 24 hpi and viral titer was
418 determined by $TCID_{50}$. D) NAV-2729 was used to pre-treat Huh7 cells 2 hrs prior infection with
419 SARS-CoV-2 (MOI of 10) on ice. NTg and ARF6-KO Huh7 cells were used as a control. 1 h

420 post infection on ice, cells were washed twice and one set was harvested in TRI reagent. The
421 second set was incubated at 37´C to allow viral internalization. One hour post incubation, cells
422 were treated with trypsin to remove bound, non-internalized virus and were harvested in TRI
423 reagent. Bound and internalized virus was determined by RT-qPCR: Graph shows % of
424 internalization over the bound fraction. N= 3 biological replicate with at least 2 technical
425 replicates, each.
426 **Figure 5.** ARF6 is critical for SARS-CoV-2 infection in more physiologic relevant cell types. A)
427 Human kidney organoids were collected and resuspended in maintenance media. Groups of four
428 organoids were infected with SARS-CoV-2 at MOI of 1. Organoids were washed twice and put
429 in culture on a matrigel-coated plate for 48 hrs. Cells were then harvested, and virus was
430 quantified by $TCID_{50.}$ Each dot represents a technical replicate of N=2 biologically independent
431 experiments. B) Calu-3 cells and Calu-3 transduced with a non-targeting guide (NTg) or ARF6-
432 targeting guide (ARF6) were seeded in 48-well plate and allowed to reach 80% confluence.
433 SARS-CoV-2 WA1 was used to infect cells at MOI of 1 for 24 hrs. Cells were then harvested,
434 and virus was quantified by $TCID_{50}$. Each dot represents a technical replicate. C) Representative
435 images (left) and quantification (right) of Calu3 transduced with a non-targeting guide (NTg) or
436 ARF6-targeting guide (ARF6) and infected with MOI of 1 of SARS-CoV-2 WA1 or SARS-
437 CoV-2 Omicron for 24 hrs. Cells were fixed, permeabilized and stained with anti-N primary
438 antibody and anti-mouse AF647 secondary antibody (N protein, magenta) and Hoechst (nuclei,
439 blue). Cells were imaged with the high content imaging platform CX5 and analyzed with Cell
440 profiler for image segmentation. Each dot represents the average of % of infected cells over 20
441 fields of image per well. Each dot represents a technical replicate.
442

443 **Supplementary figure 1:** Toxicity assay of selected drugs by Resazurin assay in Huh-7.

444 **Supplementary figure 2:** Western blot for ARF6 expression. NTg and ARF6-KO Huh-7 lysates

445 were obtained from cells seeded overnight in a 6-well plate and analyzed for ARF6 expression

446 by Western blot. A representative blot of N=3 replicates is shown.

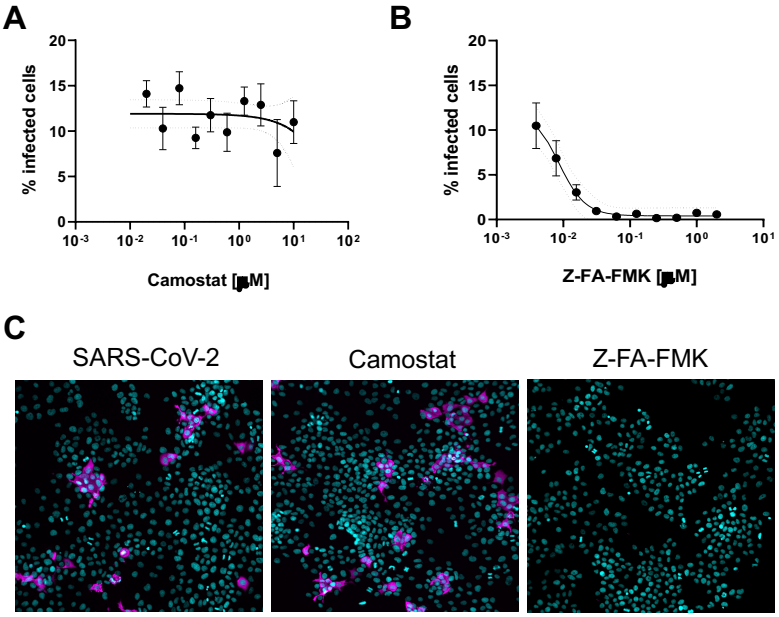
A
% infected cells
Camostat [μM]
B
% infected cells
Z-FA-FMK [μM]
C
SARS-CoV-2
Camostat
Z-FA-FMK

Figure 1

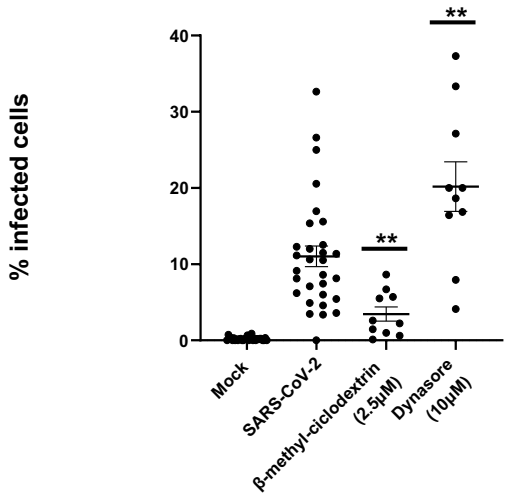
% infected cells
40
30
20
10
0
**
**
Mock
SARS-CoV-2
β-methyl-ciclodextrin (2.5μM)
Dynasore (10μM)

Figure 2

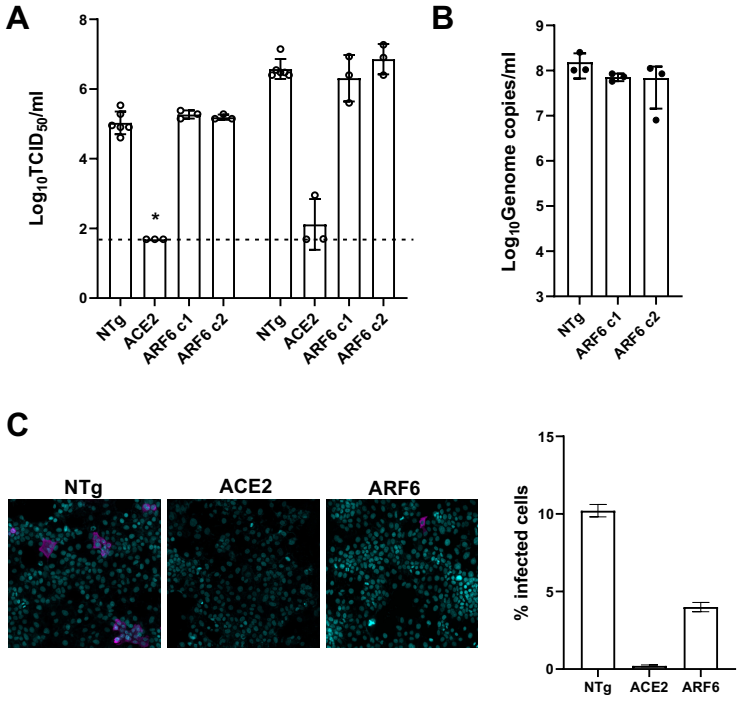
A
Log10TCID50/ml
8
6
4
2
0
*
NTg
ACE2
ARF6 c1
ARF6 c2
NTg
ACE2
ARF6 c1
ARF6 c2
B
Log10Genome copies/ml
9
8
7
6
5
4
3
NTg
ARF6 c1
ARF6 c2
C
NTg
ACE2
ARF6
% infected cells
15
10
5
0
NTg
ACE2
ARF6

Figure 3

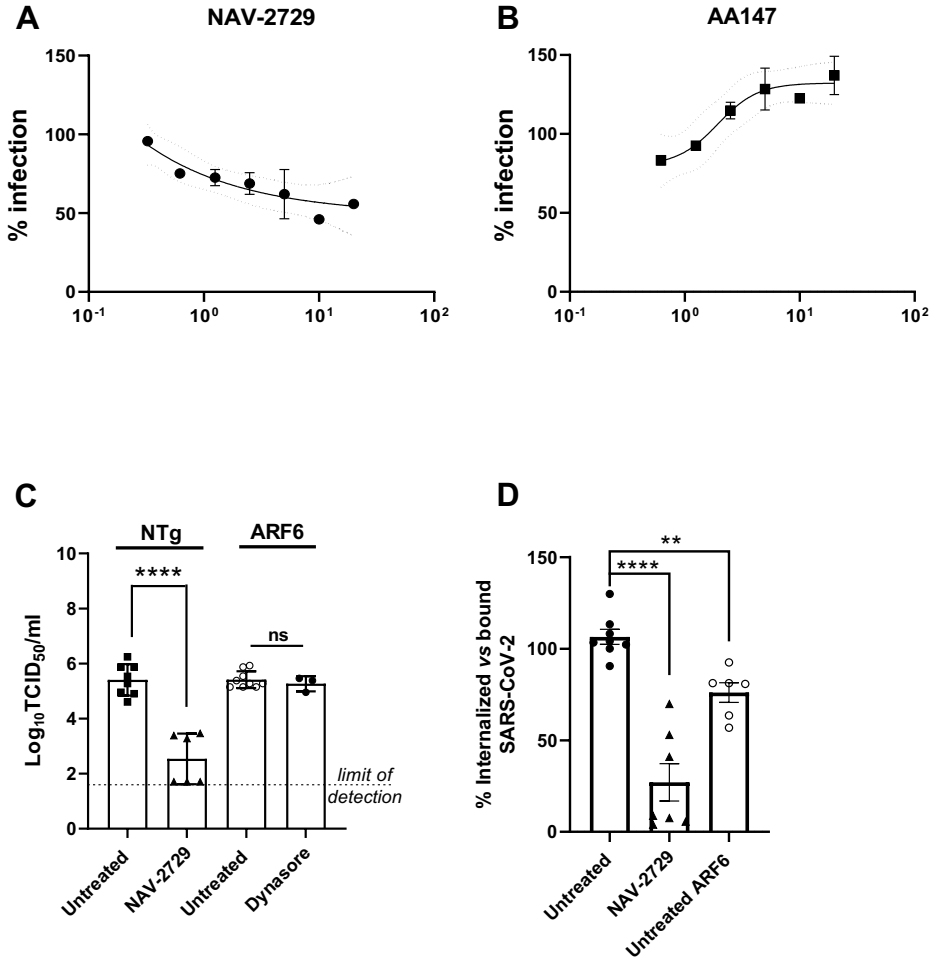
A
NAV-2729
% infection
150
100
50
0
10^{-1}
10^{0}
10^{1}
10^{2}
B
AA147
% infection
150
100
50
0
10^{-1}
10^{0}
10^{1}
10^{2}
C
NTg
ARF6
****
ns
$Log_{10}TCID_{50}$/ml
10
8
6
4
2
0
limit of detection
Untreated
NAV-2729
Untreated
Dynasore
D
**
****
% Internalized vs bound SARS-CoV-2
150
100
50
0
Untreated
NAV-2729
Untreated ARF6

Figure 4

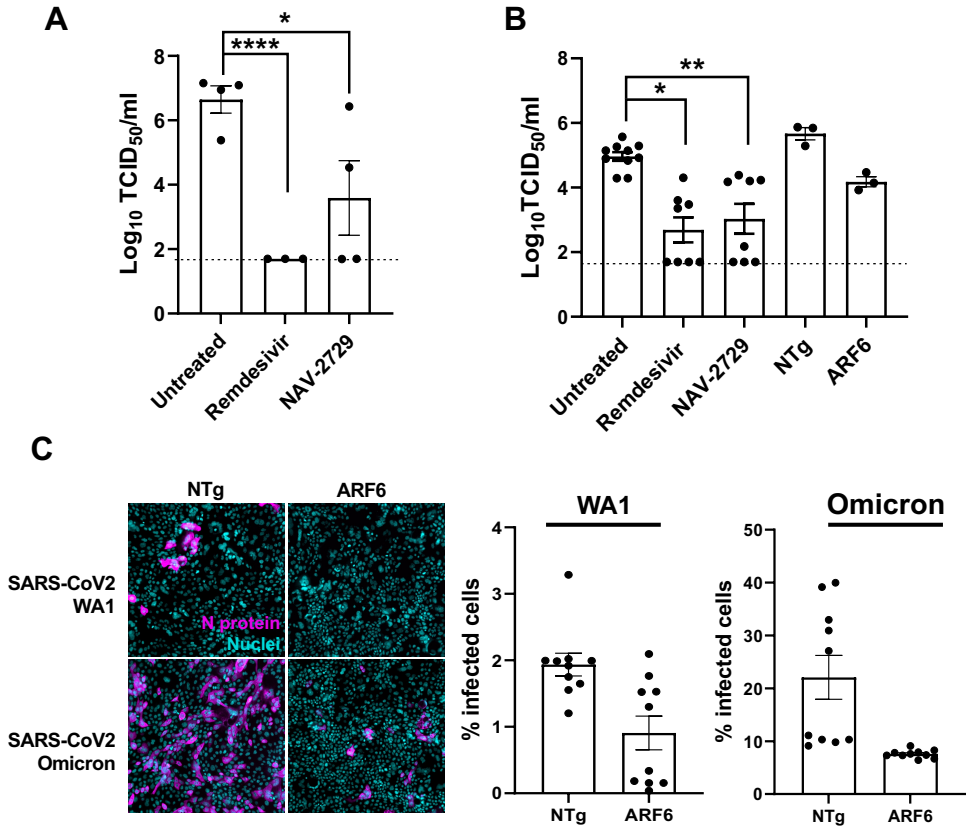
A
*
****
Log10 TCID50/ml
8
6
4
2
0
Untreated
Remdesivir
NAV-2729
B
**
*
Log10TCID50/ml
8
6
4
2
0
Untreated
Remdesivir
NAV-2729
NTg
ARF6
C
NTg
ARF6
SARS-CoV2
WA1
N protein
Nuclei
SARS-CoV2
Omicron
WA1
% infected cells
4
3
2
1
0
NTg
ARF6
Omicron
% infected cells
50
40
30
20
10
0
NTg
ARF6

Figure 5

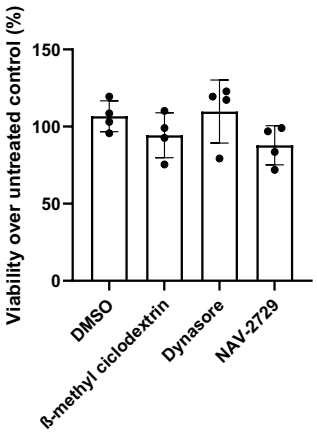

Supplementary figure 1: Toxicity of ARF6 in Huh7 cells

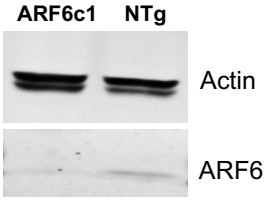

Supplementary figure 2: ARF6 Western blot